

Article type: Full Paper

Numerical and experimental analysis of high-throughput blood plasma separator for point-of-care applications

*Shadi Karimi, Mohammad Mojaddam, Sahand Majidi, Pouya Mehrdel, Josep Farre Lladós, and Jasmina Casals Terré**

Dr. S. K. Author 1, Mr. P. M. Author 4, Dr. J. F. L. Author 5, Dr. J. C. T. Author 6
Mechanical Engineering Department - MicroTech Lab., Universitat Politècnica de Catalunya,
08222 Terrassa, Barcelona, Spain.

E-mail: jasmina.casals@upc.edu

Dr. M. M. Author 2, Dr. S. M. Author 3.

Faculty of mechanical and energy engineering, Shahid Beheshti University, 16765-1719
Tehran, Iran.

Keywords: microfluidics, high-throughput, blood/plasma separation, hemostasis, POC

Abstract

Blood plasma separation from undiluted blood is an essential step in many diagnostic procedures. This study focuses on the numerical optimization of the microfluidic blood plasma separator (BPS) and experimental validation of the results to achieve portable blood plasma separation with high purity and reasonable yield. The proposed design has two parts: a microchannel for blood processing and a tank, below the aforementioned main channel, for plasma collection. The study uses 3D computational fluid dynamic analysis to investigate the optimal ratio of heights between the top microchannel and the tank and their geometry at various flow rates. Thereafter, the results are compared with the experimental findings of the fabricated devices. These results are put in contrast with some recent reported works to verify the proposed device's contribution to the improvement of quality and quantity of the extracted plasma. The optimized design is capable to achieve a 19% yield with a purity of 77.1% and depending on the requirement of the point-of-care (POC) application. These amounts could be tuned for instance to 100% pure plasma, but the yield would decrease to 9%. In this study the candidate application is hemostasis, therefore, the BPS is integrated to a biomimetic surface for hemostasis evaluation near the patients.

1. Introduction

Blood is the most important biological body fluid in clinical diagnosis and can be easily used to determine the internal performance of the human body. Red blood cells (RBC) occupy around 44% blood volume and are typically elastic biconcave discs of approximately 8 μm in diameter and 2 μm in thickness. Blood is also composed of 2% white blood cells (WBC) and Platelets. All of these components suspend in the liquid phase of blood (plasma) which is straw-yellow in color. The blood plasma occupies approximately 54% of blood volume. Plasma, besides water, contains hormones, cellular metabolism end-products, clotting factors, immunoglobulins and an abundance of proteins. These products are used as biomarkers, indicating the presence of certain diseases in an individual. [1-3] However, blood cells sometimes interfere in the biochemical readout of the results. Hence, plasma cell separation is essential in disease diagnostics. Nevertheless, separating 5 million cells per blood microliter is a highly challenging goal to achieve. [3]

In the lab environments, centrifugation is a conventional method in blood plasma separation. However, it has some drawbacks such as the amount of sample required, possible manipulation errors, the labour intensity and the operation time. Microfluidics miniaturization is an effective way to overcome the aforementioned limitations, providing the same effectiveness with a lower blood sample volume and decreasing laboratory workload. Besides, in undeveloped countries with limited access to the best medical diagnostic technologies, microfluidic systems can potentially decrease the costs associated with diagnosis by miniaturization and integration of complex functions. These systems must be portable, but also accurate, reliable, rugged and well suited to the medical and social contexts of the developing world. [1, 4]

The microfluidic plasma-separation methods have the capability of direct connection to miniaturized sensors. Thus, they can create miniaturized POC or can be embedded in small

machines for screening a large number of people in a short period (i.e. test all the passengers of a plane within 3-4 hours) at a reasonable cost.

Despite the effort of the research community in this field, there is still the issue of either low-throughput or low purity in most of the new proposed devices. [5]

This research presents a continuous separation of plasma from whole undiluted blood, enhancing a previous geometry that had evaluated to properly separate 100% pure plasma by capillary forces [6] and the electrophoretic effect. [7] The results will be compared with some of the best recent studies, which used the whole blood as mentioned in Table 1. These research works are sorted based on the yield.

In our research, firstly a BPS design is proposed by a combination of CFF and a pillar array for continuous blood plasma separation. This study investigates the optimal geometry to reach the maximum amount of the plasma extracted with the highest purity in a reasonable time. Then the optimized device is used to evaluate the hemostasis disorders in a novel portable platform.

Table 1. Research work on high-throughput separation from undiluted blood.

Study	Flow rate [$\mu\text{l min}^{-1}$]	Yield %	Purity %
Current study	166	19	77.7
[8]	3-4	15-25	99
[9]	100	12.3	93
[10]	5-30	9	100
Current study	66.6	8.5	100
[11]	904.3	5.6	99.88
[12]	33.3	5	99
[3]	300-500	1-6	99.5
[13]	500	1	80

The ability to know the level of hemostasis is essential. If the potential of the blood to clot is severely reduced, it may cause bleeding disorders such as haemophilia while over-active clotting leads to thrombosis and prevent normal blood flow through the vein or artery. [14] Conventional measurements usually include prothrombin time (PT), activated partial thromboplastin time (aPTT), fibrinogen level (Clauss method) and platelet count. One major disadvantage of these methods is the need for centralized laboratory and therefore the turnaround time. Ideally, real-time monitoring of haemostasis is required to guide drug dosage adjustments. [15] Therefore, introducing a new method that can monitor the clotting process in a shorter time with lower amount of sample and near the patients is desired.

Collagen and fibrin clots are two important factors in the wound healing process. [16] With the progressions in protein adhesion techniques in microfluidic devices, the biomimetic micro-channels can be internally coated with appropriate biological substrates, such as von Willebrand factor (VWF), collagen, Tissue Factor (TF) or fibrinogen. [17]

There is a great challenge in low-cost high-throughput devices, which will provide rapid results in near-patient settings in the field of haemostasis. The optimized microfluidic BPS is integrated to a biomimetic surface, which is coated by collagen and tissue factor for monitoring the clotting process. Future advancement of hemostatic materials and technologies can be envisioned to revolutionize bleeding treatment and transfusion medicine approaches. [18]

1.2. Principle of design

This section presents the principle of design of our microfluidic device, analysing the physics of the blood flow, and the prevailing theory of its background.

Generally, blood flow in the arteries has laminar flow characteristics and the fluid itself can be modelled as shear-thinning due to its cellular suspension. Previous researchers showed that in order to achieve axial migration of the particles and to take advantage of the inertia force in

the blood vessels, the microfluidic channel usually needs to be long, narrow and have a high flow rate. [1,3,6] In smaller blood vessels, typically with diameters less than approximately 300 to 500 μm , it is observed that RBCs tend to move toward the center of the vessel and to push other particles towards the walls of the blood vessel. This phenomenon is termed margination, also known as a cell free layer (CFL). [1] In this research, the height of the microchannel and its shape are studied to determine the influence of the aspect ratio (height/length) on the extraction.

For margination to occur, the particles need to separate their path from the fluid-flow streamlines via lateral displacements occurring due to the interaction of wall adhesion and drag forces. At low shear rates, the adhesion forces are larger than the drag forces, regardless of the particle orientation. At higher shear rates, these forces depend on the orientation of the particle. [1]

The forces exerted on a cell in a microfluidic channel are shown in Figure 1 (A). The net force acting on a cell can be expressed in equation 1.

$$\mathbf{F}_{\text{net}} = F_D \mathbf{i} + F_L \mathbf{j} + (F_B + F_g) \mathbf{k} \quad (1)$$

where F_L is the lift force in Y direction (width of the channel), F_D is the drag force in X direction (length of the channel), F_B is the buoyant force and F_g is the gravitational force in Z direction (height of the channel). Gravity facilitates the migration of the larger particles (500 nm to 10 μm) in the direction of the gravitational force.

Reynolds number defines the flow regime in microchannel as follows:

$$\text{Re} = \rho u D_h \mu^{-1} \quad (2)$$

In which u is the average velocity at channel cross-section and D_h is hydraulic diameter, defined as four times of channel cross-section area divided by the wetted perimeter. The symbol μ represents apparent viscosity, which is equivalent to dynamic viscosity in Newtonian fluids and zero-shear rate viscosity in the case of shear-thinning fluids.

Since Reynolds number is typically low, the drag force can be expressed as follows [1,19] :

$$F_D = -6 \pi R \eta (v_f - v_p) \quad (3)$$

where R is the radius of the particle, η is the viscosity of the fluid, v_f is the velocity of the fluid flow, and v_p is the velocity of the particle. The buoyant force acting on a spherical particle suspended in a fluid can be expressed as follows:

$$F_B = 4 \pi R^3 \rho_f g \quad (4)$$

where, ρ_f is the density of the fluid, and g is the acceleration due to gravity. The gravitational force acting on a spherical particle is expressed as follows:

$$F_g = 4 \pi R^3 \rho_p g \quad (5)$$

In which, ρ_p is the density of the particle. The gravitational and buoyant forces only act in the vertical direction on the cell, whereas the drag force acts in the direction opposite to that of the flow-stream. In human blood, the density of the plasma is smaller than that of the RBCs, WBCs, and platelets. Thus, all the blood cells sink as the fluid flows in the microfluidic channel. Thus, clogging can be occurred at the entrance of the extraction channel in capillary-based setups. [12]

The lift force leads to migration across the streamlines. In the expansion structure of the microchannel where the streamline changes direction smoothly, a particle is primarily subjected to the shear-gradient lift force (FLs). As it is shown in Figure 1 (A), FLs is arising from the curvature of the Hagen-Poiseuille flow and acts downward and parallel to the velocity gradient and drives the particle towards the channel walls. On the other hand, the wall-effect lift force (FLw) acts upward and parallel to the velocity gradient and pushes the particle away from the wall toward the channel centerline; the net force of these two forces is the lift force (FL) that is responsible for particle migration away from the wall.

This lift force can be calculated by [1,19] :

$$F_L = \mu \gamma \cdot r^3 h^{-1} f(1 - v) \quad (6)$$

Where $\dot{\gamma}$ is the shear rate, r is the radius of the particle, h is the particle's distance from the wall and $f(1 - v)$ is a dimensionless function based on the reduced particle volume and is given by:

$$V = v (4 \cdot 3^{-1} \pi (S (4\pi)^{-1})^{1.5})^{-1} \quad (7)$$

where V is the enclosed volume and S is the surface area of the particle. [1]

Generally, the discoidal shape of RBCs, combined with their elasticity and membrane fluidity, results in strong lift forces that push RBCs toward the center of the channel and lead to the formation of a CFL.

To find the optimum geometry and flow rate to maximize the CFL and allow the maximum extraction of plasma, besides the main channel height, the main channel geometry is numerically analysed to study the different gradients generated on the flow profile and how this can enhance the plasma extraction.

Flow properties and therefore CFL thickness is influenced by channel geometry and particle size. In this study the particle size is kept constant. [1] But a parametric analysis is performed to evaluate the influence on yield and purity of the channel geometry and cross-section aspect ratio.

Figure 1 (B) illustrates the schematic view of the analyzed BPS designs consisting of two parts. The top part, made out of PDMS, comprises the main channel, two plasma collector channels and a bottom part made out of an etched glass. The three different geometries proposed for the main channel (CS: Stand for Channel Shape) are corrugated (C), straight (S) and lopsided (L) as shown in Figure 1 (C) c, d, e respectively. The etched glass is a tank to collect the extracted plasma which includes an array of pillars (PS: stand for pillar shape) (Figure 1 (C) a, b) in order to hold the load of the PDMS part. Two designs are considered for pillars; elongated bars (B) and diamonds shapes (D) but in the numerical investigation, a tank without pillar (O) is also studied. The depth of the tank is adjusted to be lower than the minimum size of the RBCs (2 μm) to prohibit the escaping of cells from the main channel

into it. The influence of the depth of the tank PS (h) is examined for three different values of 1.2, 1.5, and 1.8 μm . The height of the main channel (H) is also studied in order to evaluate the influence of aspect ratio on the yield of the separation. The suggested values are 16, 25, 45 μm . eventually, to facilitate the comparison of the cases each geometry named using a 4-tuple like (H, h, CS, PS) which shows the characteristics.

When the blood flow, while passing through the main channel, finds its way downward to the etched tank, all the accompanying cells are filtered out due to their size. Thus, a layer of pure plasma is formed in the tank and is collected by two plasma collector channels.

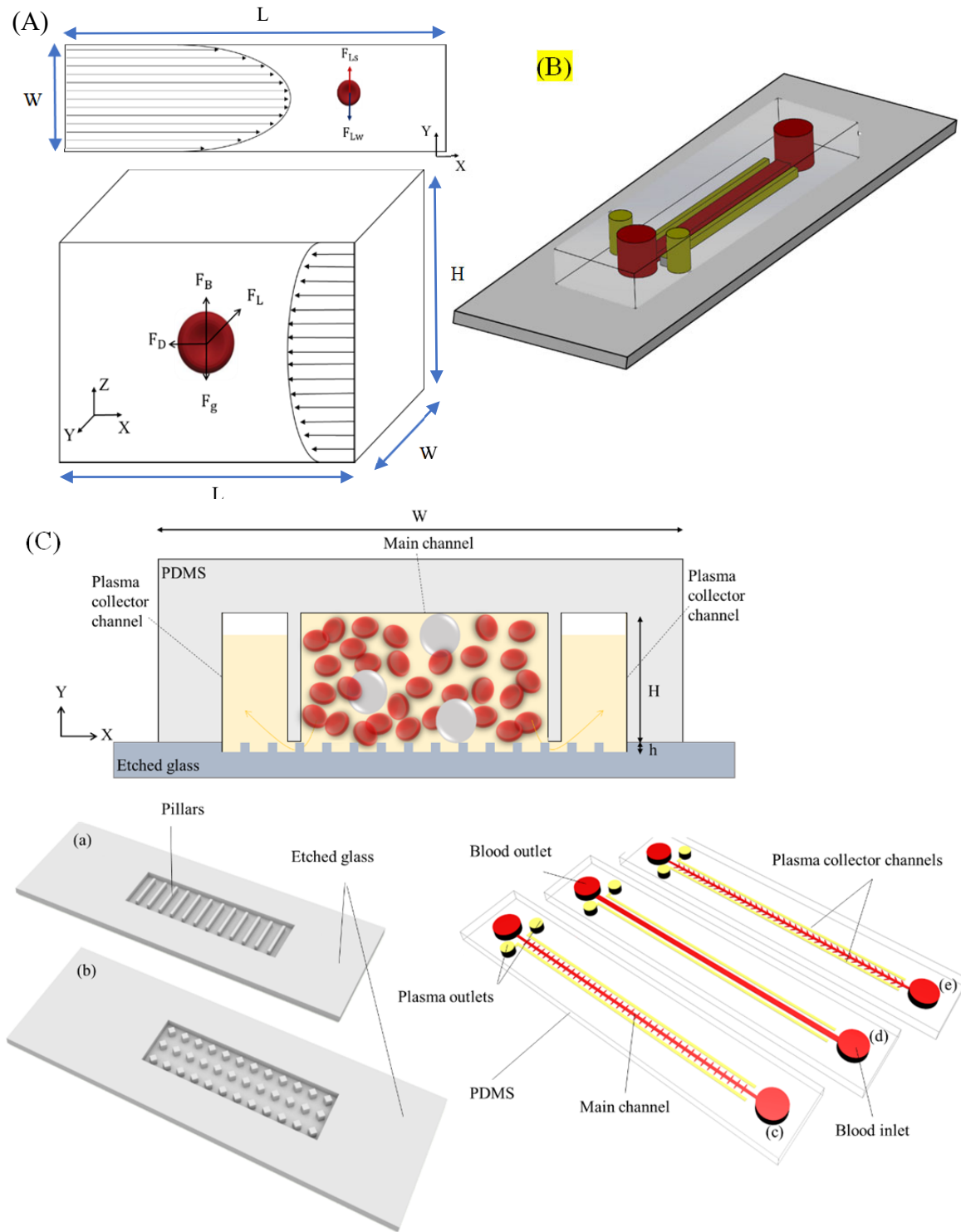


Figure 1. (A) The schematic the forces exerted on a single cell in a microchannel. F_{Ls} is the shear gradient lift force and F_{Lw} is the wall induced lift force and F_L is the net lift force, F_D is the drag force, F_B is the buoyant force and F_g is the gravitational force. Width, length and height of the channel are shown by W , l and H respectively. (B) schematic of the complete BPS which contains a PDMS block on the top part, named as CS parameter and an engraved glass on the bottom part named as PS parameter. (C) the cross-section view of the BPS during separation, (a) etched glass with elongated bar pillars named as B, (b) etched glass with diamond pillars named as D, and for the numerical study a case without pillars also considered which named as W, (c) PDMS with a corrugated channel named as C, (d) PDMS with straight channel named as S, (e) PDMS with a lopsided channel named as L.

1.3. Fabrication

The two sections of the BPS, i.e. PDMS and etched glass, are fabricated separately. [20] The etched glass is fabricated according to the standard wet-etching process to create a tank with the pillar array in the glass. The PDMS, on which the microchannel carved by the aid of mold, is manufactured utilizing the conventional standard soft-lithography procedure. These two parts are bonded via oxygen plasma. Further information regarding the details of the fabrication process is mentioned in appendix, *fabrication section*.

2. Materials and methods

2.1. Modeling

Continuity and momentum equations are solved to study the fluid flow behavior and prediction of the main flow characteristics. Considering incompressible flow, the general governing set of equations are reduced to Equation 8 and Equation 9 respectively:

$$\nabla \cdot \mathbf{V} = 0 \quad (8)$$

$$\rho (D(\mathbf{V})/Dt) = -\nabla p + \mu \nabla^2 \mathbf{V} + \mathbf{g} \quad (9)$$

In which, D/Dt indicates the material derivative, \mathbf{V} is the velocity vector, μ indicates viscosity, ρ indicates density, and p represents pressure. The gravitational force is the only volumetric force present in this study and is represented by \mathbf{g} .

A three-dimensional solver, ANSYS FLUENT 19.2, is utilized for performing the numerical study. Steady state flow is considered and SIMPLE algorithm is used to handle pressure-velocity coupling.

The fluid is considered as a single-phase liquid with density of 1060 [kg m⁻³], viscosity of 0.0032 [Pa s] and is modelled as both Newtonian and shear-thinning.

The flow regime can be determined using Reynolds number (equation 2). Considering the channels dimensions and the average velocity for different models, $Re \ll 1$ and a laminar

creeping flow is ensured in this study. From equation 9, the symbol μ_0 represents apparent viscosity, which is equivalent to dynamic viscosity in Newtonian fluids and zero-shear rate viscosity in the case of shear-thinning fluids. The shear-thinning behavior is resembled by power-law model in which local fluid viscosity obeys the following equation.

$$\mu = \min (\max (\mu_{\min}, K\dot{\gamma}^{n-1}), \mu_{\max}) \quad (10)$$

In equation 10, K is the consistency factor as a measure of the mean fluid viscosity and is set equal to 0.42Pa.s^n . Symbol n is the power-law index, which determines deviation from Newtonian flow behavior and is set equal to 0.61 [9]. In addition, parameters μ_{\min} and μ_{\max} are lower and upper bounds for viscosity variation, respectively. The parameter $\dot{\gamma}$ represents shear-rate and it is defined to be a function of velocity gradients.

Due to symmetry, half of the geometry is modeled and for simplicity the cylinders of the inlets and outlets are not included.

The boundary conditions are set considering one inlet and two outlets. Mass flow rate is set at the inlet and the zero relative static pressure is set at the main as well as the lateral outlet (the symmetrical geometry contains one lateral outlet).

Symmetry boundary condition is imposed on the plane of symmetry. Walls are considered to be adiabatic with no slip condition.

Spatial discretization of convective terms is performed using monotonic upwind central scheme for conservation laws (MUSCL) which is a blending of central and second order differencing schemes as given in below.

$$\phi_{\text{MUSCL}} = \theta \phi_{\text{central difference}} + (1-\theta) \phi_{\text{second order upwind}} \quad (11)$$

In equation (11), θ is a blending factor with its interval between zero and one and its value is determined locally to avoid formation of local extremes in the solution. Diffusive terms are discretized using central differencing method. The convergence reached when the root mean square of conservation equation residuals is reduced to $1\text{e-}5$.

2.2. Geometry and grid generation

Structured hexahedral grid is used to reduce the mesh size and thus computational cost while maintaining the appropriate grid quality. As the main channel height, H is one order greater than the height of pillars, h , it is important to tailor the meshes in this zone to have enough cell layers and capture the flow characteristics correctly. Considering 5 to 7 mesh layers in the etched part (at average 1.5 micron in thickness) increases the total mesh numbers significantly as the mesh aspect ratio limits has to be met. More refinement is applied for the zones with the sharp angles and for the small curved areas especially in corrugated and lopsided geometries. The figure of our grids is available in appendix, *simulation section*.

Mesh independency is assessed for different main channel shapes to ensure the accuracy of the model. Pressure drop from inlet to outlet is considered for this study. The results for the case ($H = 25 \mu\text{m}$, $h = 1.8 \mu\text{m}$, $CS = C$, $PS = W$) are also shown in *simulation section* of appendix. Average cell size is sequentially halved until the pressure difference become independent from the grid sizes. The independency is reached for cases with mesh number equal to 5 million and above. Thus, the cell size corresponding to the case with around 5 million cells is chosen for the numerical investigation.

2.3. Experiments

2.3.1. Materials

In order to make the microfluidic BPS

2.3.1. Biological validation

Two parameters are monitored: purity and yield. For the purity analysis, a protocol developed by our research group [6] compares the number of RBCs in an area of the main channel and the plasma collector channel. These areas are captured by microscope (Tucsen ISH500, Tokyo, Japan) with a micro inspection lens system (Optem zoom 125C with a broad 12.5:1 zoom range and a 20X objective) and an image processing is developed by an open source

ImageJ software. See appendix, *experiments section*. In this study, the number of blood cells in the plasma collector channel is counted and compared with that of the blood cells in the main channel as expressed in the following.

$$\text{Purity \%} = (1 - (\text{final cells density} / \text{initial cells density})^{-1}) \cdot 100 \quad (12)$$

The yield of the BPS is obtained from equation 13.

$$\text{Yield \%} = (\text{output sample volume} / \text{input sample volume})^{-1} \cdot 100 \quad (13)$$

The biomimetic surface is first coated with paraformaldehyde 1% for 15 min at 4 °C to analyze the results and then incubated with glycine 1% for 10 min at 4 °C. This is for reducing the staining background created from free unreactive aldehyde groups. Later the surface is fixed with 1% bovine serum albumin (BSA) for 15 min before incubation with antibodies.

In order to integrate the direct and indirect immune-fluorescence, firstly in a humidified chamber, the platelets are stained with a mouse anti-CD36 primary antibody at room temperature (37 °C) for one hour. Secondly, a conjugated antibody anti-fibrinogen Alexa Fluor 594 is incubated with a secondary antibody anti-mouse Alexa Fluor 488 also at 37 °C and for one hour in a humidified chamber.

Microscopic images are captured with a confocal microscope (SP5, Leica Microsystems, Barcelona, Spain). The images are analyzed using the ImageJ software (v 1.43m).

In the photos, platelets are in green and fibrins are in red. Co-distributions between them is measured by comparing the percentage of covered surface corresponding to each marker. [21]

2.3.2. Experimental setup

Fluidic control is achieved using a programmable in-line pressure syringe pump (Graseby 3200 Smiths, Watford, Hertfordshire, United Kingdom) that is connected to the blood inlet to generate a uniform flow rate. A 5 ml syringe is connected to a pneumatic chamber through air-tight plastic peek tube and pushed from 5 ml to zero to apply a high pressure at a precise

and stable flow rate [1 ml h^{-1}]. The inner pressure at this flow rate is 29.5 kPa that is below the maximum pressure that the bonded PDMS is able to resist. The assembled device is placed on a movable platform under the microscope that is connected to a computer for picture capturing. See appendix, *experiments section*.

2.3.3. Sample preparation

Whole blood samples in this study are drawn from healthy donors in Hospital Mutua de Terrassa and collected in a 5ml anticoagulant vacutainer. The blood is used within a maximum of 4 days after donation and is stored at 4 °C.

2.3.4. Biomimetic surface preparation

In order to prepare a biomimetic surface, the glass slides ($18 \text{ mm} \times 18 \text{ mm} \times 1 \text{ mm}$, from Delta Lab) are cleaned via piranha cleaning technique [21] and functionalized with collagen Type I (Chronology Corp. Havertown, PA, USA) and tissue factor (Innovin, Siemens, Madrid, Spain) at Hospital Clinic of Barcelona. The coating concentrations is equivalent to 30.9 mg/cm^2 for collagen and 0.95 ng/cm^2 for tissue factor. Functionalized slides are stored at 4 °C overnight and flushed with saline solution right before the experimental test to eliminate the remaining collagen over the surface. [21]

3. Results and discussion

3.1. Simulation

A parametric study of the different models is performed to identify the optimized geometry. Since the CFD simulations are performed using a single-phase fluid model, the effect of the geometry on velocity, pressure drop from inlet to outlet (ΔP) is captured. Furthermore, the numerical yield (Y_N) ratio is obtained using the following definition.

$$Y_N = (\text{Lateral Flow Rate}) (\text{Inlet Flow rate})^{-1} \quad (14)$$

3.1.1. Straight channel

Table 2. The straight channel cases for comparison.

Case	Geometry
1	($H=25\mu\text{m}$, $h=1.2\mu\text{m}$, $CS=S$, $PS=W$)
2	($H=25\mu\text{m}$, $h=1.8\mu\text{m}$, $CS=S$, $PS=W$)
3	($H=45\mu\text{m}$, $h=1.8\mu\text{m}$, $CS=S$, $PS=W$)
4	($H=45\mu\text{m}$, $h=1.8\mu\text{m}$, $CS=S$, $PS=B$)

Main channel height, H

Referring Table 2 the yield and ΔP are compared for the Cases 1 - 4 by considering Case 2 as the reference. The results are shown in Figure 2 (A). The effect of H is captured through comparing two models with $H = 45 \mu\text{m}$ and $H = 25 \mu\text{m}$ with other geometrical parameters remaining the same (H , $h = 1.8 \mu\text{m}$, $CS = S$, $PS = W$). The case with $H = 25 \mu\text{m}$, as illustrated in Figure 2 (A), guides 1.74 times more flow to the lateral channels. For straight channel, as it is expected by decreasing the main height, much more flow is directed to the etched part, hence the lateral channel mass flow rate increases but the pressure drop also increases significantly.

Etched part height, h

The effect of h is captured through the comparison of two models: $h = 1.8 \mu\text{m}$ and $h = 1.2 \mu\text{m}$ with other geometrical parameters remaining the same ($H = 25 \mu\text{m}$, h , $CS = S$, $PS = W$). In case with $h = 1.8 \mu\text{m}$, the pressure drop is less (about 23% in this case) than in $h = 1.2 \mu\text{m}$. Figure 2 (A) shows that the Y_N for the case $h = 1.8 \mu\text{m}$ is 1.42 times more than the flow with $h = 1.2 \mu\text{m}$.

Pillars

The presence of pillars definitely increases the pressure drop; however, they are structurally necessary to bear the weight of the PDMS block. The second reason is to help blood cell separation as it prohibits the direct flow of the blood through the outlets and guides the flow to the lateral channels, thus increasing the separation. The other reason is related to the micro device manufacturing as the pillar ensures a relatively constant distance between the PDMS layer and the etched tank. However, in numerical simulation adding pillars increases the pressure loss as it increases the surface friction causing higher ΔP .

Two cases with and without pillars $PS = B$ and $PS = W$ are compared with this characteristic: ($H = 45 \mu m$, $h = 1.8 \mu m$, $CS = S$, PS). Yield in $PS = B$ is decreases by 50% related to $PS = W$ and ΔP increases about 22%.

To compare the quality of the flow in the etched part, the axial velocity of the flow in the plane situated 0.6 micron below the main channel is captured for the mentioned cases, see Figure 2 (B). The cases with higher mean axial velocity results in better yield, however the trend shows how the separation occurs in the whole length of the micro channel. It should be mentioned that for case 4, the existence of elongated bar pillars at the etched tank causes zero

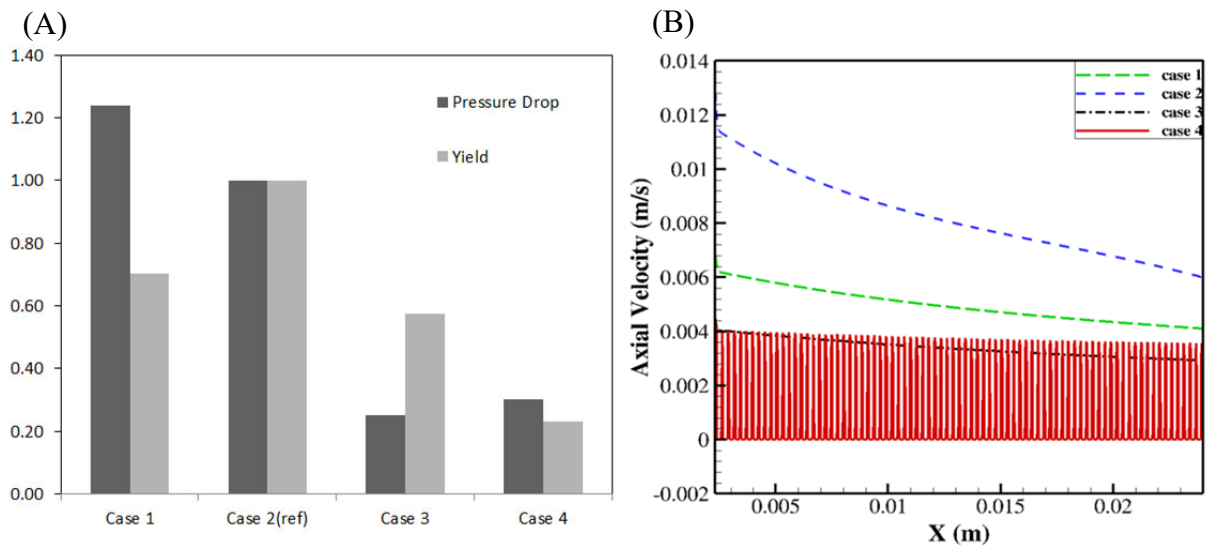


Figure 2. (A) Comparing yield and pressure drop for straight channel models. (B) Comparing the axial velocity in all four cases of table 2.

values in the axial velocity.

3.1.2. Corrugated channel

Case 1 has a top straight channel, Case 2 and Case 3 have a corrugated configuration as tabulated in Table 3, and Case 4 contains diamond pillars at the etched tank.

Table 3. Comparing Corrugated Channel results.

Case	Geometry
1	$(H=25\mu\text{m}, h=1.8\mu\text{m}, CS=S, PS=W)$
2	$(H=25\mu\text{m}, h=1.8\mu\text{m}, CS=C, PS=W)$
3	$(H=16\mu\text{m}, h=1.2\mu\text{m}, CS=C, PS=W)$
4	$(H=16\mu\text{m}, h=1.2\mu\text{m}, CS=C, PS=D)$

The geometry design of the main channel can take advantage of the hydrodynamic flow behavior to improve blood plasma separation if the wet perimeter of the top channel is increased compared to a simple straight channel. The longer perimeter provides more space for releasing plasma and creating a CFL. Previous work from our group showed that a presence of a dead-end zone on the blood transport channel helped to enhance the throughput of the device by capturing some RBCs. [7]

In the upper layer, as it can be seen in figure 3 (A), the flow velocity is decreased around the centerline of each tooth (Figure 3 (A) compares the case 1 and the case 2 from Table 3). As it is discussed earlier in the principle of design, the lift force is the reason for migration across the streamlines. In the expansion structure of the microchannel where the streamline changes direction smoothly due to the oscillation of the velocity along the main channel, the particles move towards the channel walls, while the wall effect lift force pushes them away from the wall toward the channel centerline. The stream in the main channel also flows mainly to the etched part through the corrugated teeth and then pours in lateral channels. Since in the

straight channel case, the lateral velocity along the centerline is constant and zero therefore the corrugated case seems to be a better candidate for plasma extraction by offering more space to release plasma and accelerate the flow. Adding diamond pillars to the etched part (case 3) decreases (5%) the yield in the case 4. However, these pillars are necessary to prevent the collapse of the top PDMS layer causing the blockage the etched part as mentioned earlier. Figure 3 (B) shows the axial velocity in the plane in 0.6 micron below the main channel based on the defined cases 1 and 2 in Table 3. The axial velocity in the etched part inherits the periodic trend from the corrugated upper layer. The comparison of case 1 and case 2 shows that case 2 is a better candidate for plasma extraction. In case 2 (corrugated geometry), due to the longer perimeter and more space for releasing plasma and the creation of increased CFL, the Numerical yield is more than case 1. Comparing cases 2 and 3 in which the layer heights

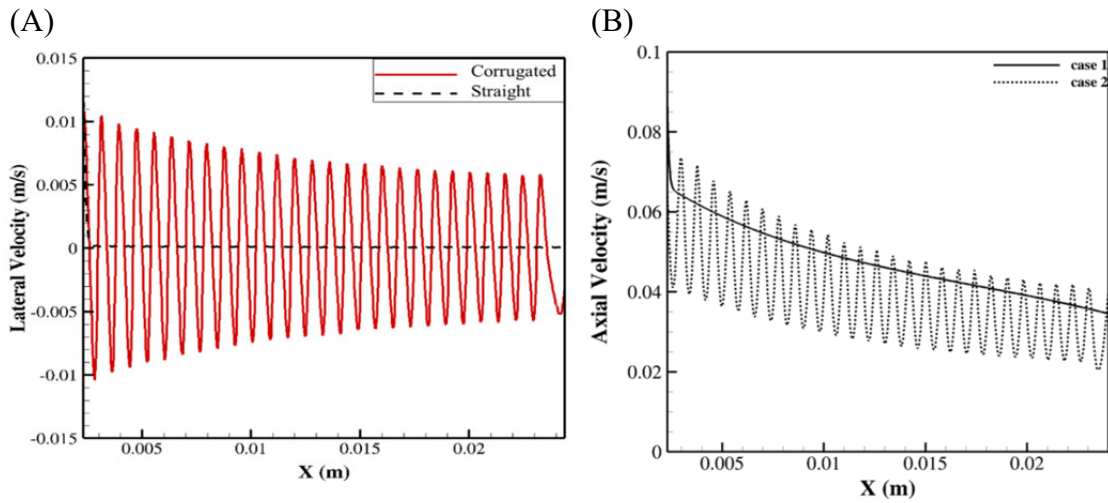


Figure 3. (A) comparing lateral velocity magnitude for corrugated and straight channels, (B) comparing the axial velocity in two cases of corrugated and straight channels.

are different, confirms that the results agree with the results from straight channel cases: 1 and 2.

3.1.3. Lopsided channel

Lopsided geometry has been named as the geometry of main channel with inclined teeth. A model with this characteristic is created and tested: ($H = 25 \mu\text{m}$, $h = 1.8 \mu\text{m}$, $CS = L$, $PS = B$). Incorporating bar type pillars in the lopsided configuration results into a complicated geometry for mesh generation. The main challenge is generating structured grids in the upper and lower layers of the geometry with an exact matching of the computational cells at the interface of the two grid sets.

The static pressure contours inside the main channel indicate that the pressure is decreased from the inlet to the outlet. In order to study the fluid motion in the etched part, the area along the main channels is divided into four separate zones and the mass flow rate in each part is calculated. According to the results, the section closest to the inlet of the device, extracts 50% of the flow. Consequently, in the new design, the plasma outlet is displaced from its original position near the blood outlet and is located near the blood inlet to improve the extraction. This analysis also shows that the etched part could have two converging edges towards the outlet with decreasing the distance between the plasma collector channel and the main channel.

In this case, the pressure drop is approximately similar to the model with the corrugated teeth shape while the yield is slightly improved due to the declined teeth, which are more in favor of the flow direction. The streamlines for the lopsided case show that the fluid flow covers almost the whole teeth whereas in corrugated channel half of the space is empty. The figures of this study are available in appendix, *results section*.

3.2. Experiments

In this section, the results obtained from 10 different fabricated devices at different flow rates are compared with the numerical results.

3.2.1. Straight channel

According to Figure 4 (A), the experimental results for the straight channel with diamond pillars at a flow rate of 4 [ml h⁻¹] shows that the achieved purity for all the cases is about 100%, while with increasing the tank's depth the yield increased. This trend agrees with the numerical results. Therefore, the depth of the etched tank should be kept as high as possible but not higher than 2 μ m. The numerical results also show that avoiding pillars would significantly improve the yield. Besides, in the experimental case, these pillars are essential to hold the weight of the flexible PDMS and avoid the collapse in the system. To make this pillar-free design possible, the manufacturing method should be changed. Moreover, Figure 4 (B) demonstrates the main channel's height effect. It is seen that at a constant flow rate of 4 [ml h⁻¹] with decreasing the height of main channel height, the yield will increase in agreement with the numerical models. By decreasing the main channel height, the pressure at the main channel will increase pushing the fluid to the etched part. Therefore, the configuration with the lowest main channel height is the best candidate for the final design.

It is fair to mention that the difference between the experimental and numerical results in Figure 4 is due to the presence of particles in the experimental case. Particles increase the flow resistance and consequently decrease the yield. In the numerical simulation, the particles are neglected to avoid further complexity in the numerical model and the unnecessarily imposed computational cost. Since the density of the particles in blood is lower than the density of plasma, the particles would follow the streamlines. The experimental results should follow the same trend as the model.

3.2.2. *Corrugated and lopsided channel*

By increasing the flow rate (above 7 [ml h⁻¹]), the purity decreases but it is still reasonable. For instance, for the case ($H = 16$, $h = 1.8$, $CS = C$, $PS = D$), there is 91.5% purity at the flow rate of 10 [ml h⁻¹].

According to the numerical results, the corrugated and lopsided channels generate a flow path that will direct the particles (RBCs) to the sides.

3.2.3. Elongated bar pillars

For high-throughput applications, the top part currently manufactured in PDMS had to be thick enough to be able to connect the syringes pumps via pipes to the inlet and the outlets. A thicker PDMS layer increases the chance of collapsing. To prevent the possible collapse, initially diamond shaped pillars have been replaced by elongated bar pillars. The fabricated device is

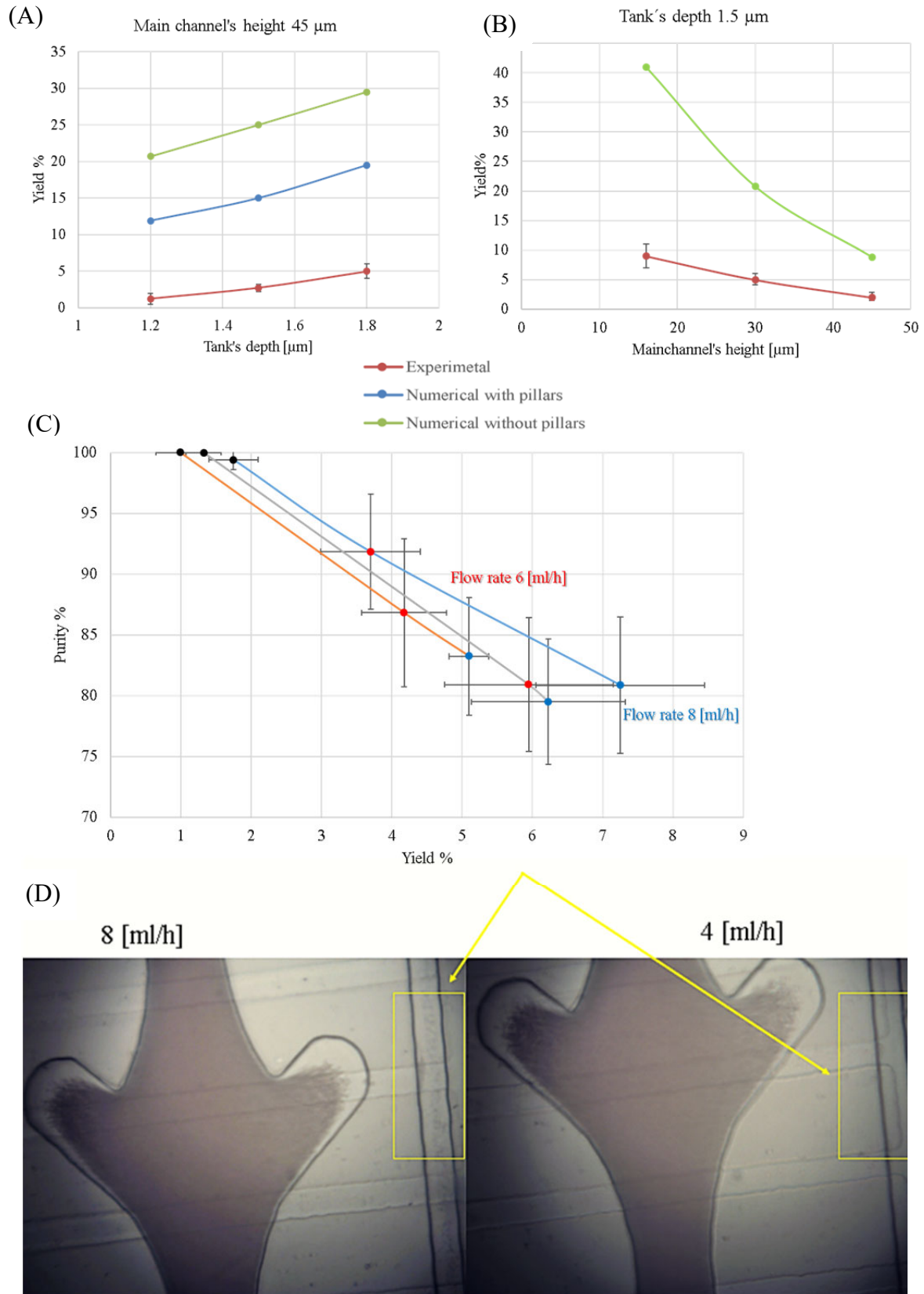


Figure 4. The comparison of the results from experimental tests and numerical studies on the yield at (A) different tank's depth, and (B) different main channel's heights, (C) comparison of yield vs. purity for three different main channel design at different flow rates, (D) experimental photos of the BPS (elongated pillars and lopsided channel with 1.8 μm depth and 45 μm height) at different flow rates for purity comparison.

tested at four different flow rates. Figure 4 (C) shows the comparison of purity versus yield at different flow rates. The results show that the lopsided channel is a better candidate compared to the straight and corrugated channels. At a low flow rate of 1 [ml h⁻¹], the yield decreases compared to the same device with diamond pillars. However, at a high flow rate, the yield significantly increases and the purity decreases, see Figure 4 (D). This is due to the high pressure inside the channel which forces the cells to stretch and escape from the main channel. Since PDMS is flexible, this pressure might deform the main channel and allow the particles to penetrate to the plasma channel.

The results of our optimized device ($H = 16$, $h = 1.8$, $CS = L$, $PS = B$), at two different flow rates, 4 and 10 [ml h⁻¹] are mentioned in table 1. According to the results, this design is the most suitable for achieving the highest purity and yield respectively. These results are compared with the results from the recent literature, mentioned at the introduction section in Table 1. Based on the results, the proposed optimized device extracts 8.5% of plasma at a flow rate of 4 [ml h⁻¹] with the highest purity: 100%. Additionally, at the flow rate of 10 [ml h⁻¹] the device separates 19% plasma with the purity of 77.7%. These variations can be attributed to the change of CFL thickness at different flow rates. The CFL layer is thicker for higher flow rates since the lift force pushes the particles further away from the wall. The whole process takes about 10 min from the sample load to the output sample extraction.

One of the significant properties of these devices is that they are clog-free. Furthermore, they are reusable after cleaning with the required procedure. Nevertheless, to avoid a possible cross-contamination for the sensitive biological cases, it is suggested to use a new device for each test.

4. Hemostasis evaluation

The proposed BPS can potentially be utilized in those applications that work with high-throughput plasma to create a POC applications. As it is explained before in this work we evaluated the hemostasis level in the extracted plasma. The proposed BPS is connected to a biomimetic surface and create a miniaturized diagnostic system for hemostasis evaluation which provides the monitorization of the interaction of platelets and fibrin components in blood clotting by differentiating the number of platelets in the plasma. The other approaches [22-24] for hemostasis evaluation usually are time-consuming and perform under static conditions. This platform can provide a tool to improve the knowledge of hemostasis process, not only in short and real-time but also with lower volume of samples. Figure 5 shows the

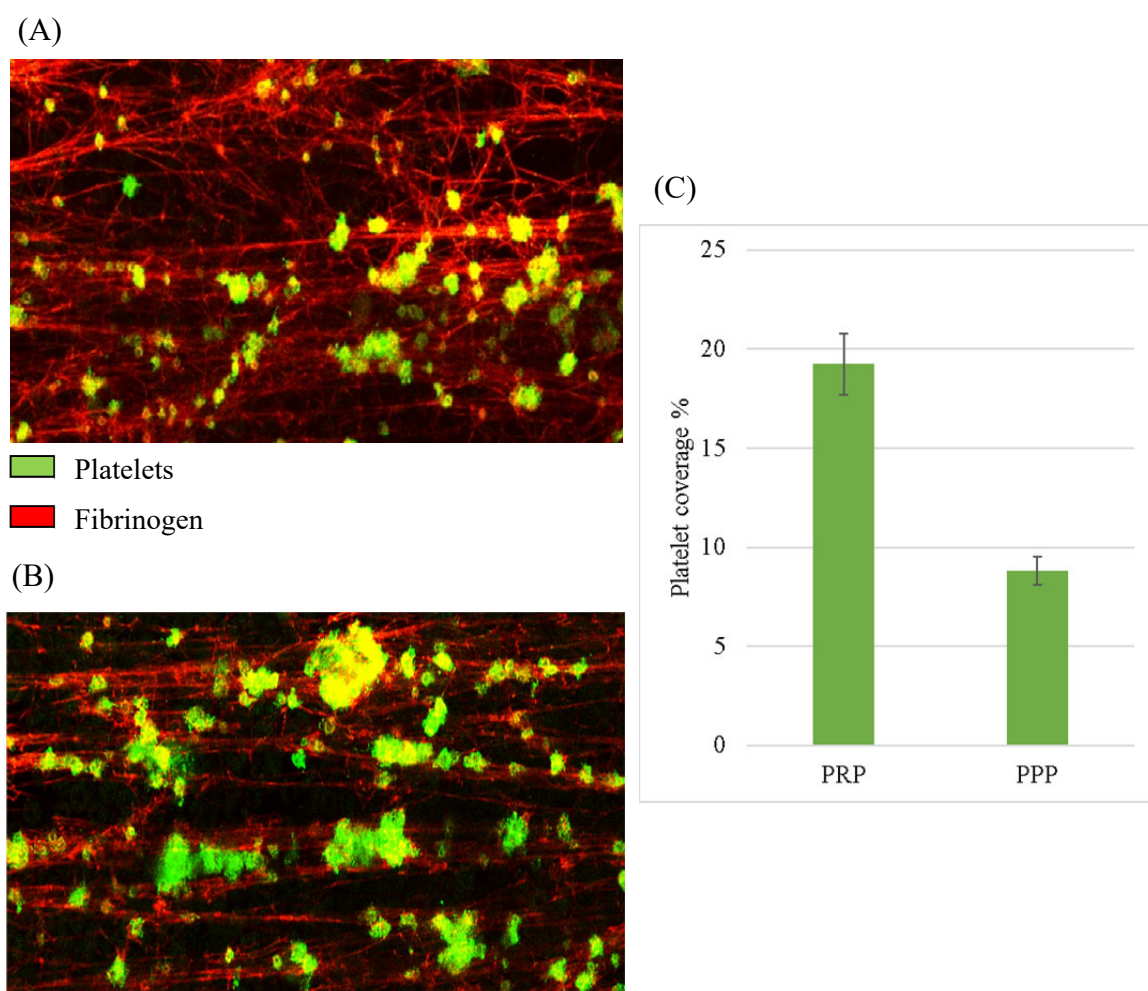


Figure 5. Confocal microscopy of the biomimetic surface presents the platelets which are labeled with byanti-CD36 Alexa Fluor 488 and fibrinogen that is labeled by anti-fibrin(ogen) Alexa Fluor 594, (A) PPP (B) PRP, (C) the graph shows the quantification of platelet aggregates in green and fibrinogen in red interacting with the collagen/tissue factor surface. (C) This graphs in the right panel summarize the results as percentages of the total surface exposed by platelets for to cases of PPP and PRP.

confocal image labeled by immunofluorescence for morphometric analysis on the biomimetic surface which illustrates the distribution of platelets in green and fibrinogen in red that interact with collagen-tissue factor surface as explained in experimental setup. Figure 5A is a sample of platelet-poor plasma (PPP) and Figure 5B shows a sample that is platelet-rich plasma (PRP). In order to distinguish between these two samples, the surface that is covered by platelets is measured for both samples which is presented in a graph of Figure 5C. As it was expected the sample of PPP has lower number of platelets interacted with fibrin compare to PRP. To perform this test only 100 μ l of plasma needs to be extracted from the whole blood. Therefore, less than 1 ml blood is required and the whole evaluation process takes maximum 6 minutes. In comparison with the other methods, mentioned in the introduction, not only the required sample and time are reduced but also the test is performed under real time condition.

5. Conclusion

A design of high-throughput BPS device has been numerically optimized and experimentally validated. As reported by the results, lowering the height of the main channel leads to the higher yield due to the increase in pressure and Reynolds number in the main channel. While increasing the depth of the etched tank, especially in the presence of pillars, induces the yield and reduces the purity. The lopsided channel shows a slight improvement in yield compare to the corrugated and straight channels. The model behavior is validated, though due to the assumptions, the reported model yield is generally higher than the experimentally obtained. Furthermore, the experimental results, in agreement with the model, demonstrate that the proposed device can efficiently separate plasma from undiluted blood in a simple way and continuous process.

The proposed design is suitable for two different scenarios: If high purity is essential, the configuration with diamond shaped pillars and 1.8 microns in height can be used at low flow

rates. Whereas, when a higher yield is important, the use of 1.8-micron elongated bar pillars is better. This device is reusable and cost effective, therefore, it is expected to be a practical tool for blood separation and analysis. Hemostasis evaluation is used as an application for the extracted plasma. Combination of a microfluidic BPS and a biomimetic surface, leads to a reduction in the required samples and time. This study serves as a base for a POC device capable of evaluating the hemostasis near the patient by measuring on platelet aggregation.

Supporting Information

Appendix.

Acknowledgements

This research was funded by Spanish Ministry of Economy and Competitively, grant numbers CTQ2017-84966-C2-1-R and CTQ2016-77936-R.

Compliance with Ethical Standards

The authors declare that there is no conflict of interest. All co-authors have seen and agree with the contents of the manuscript and there is no financial interest to report. The studies have been approved by the Comitè d'Ètica de la Universitat Politècnica, under the supervision of the Vice-Dean of Research. The studies have been performed according to the Declaration of Helsinki, therefore, all individual participants had signed the informed consent. All individual participants blood samples were obtained from the Catalan Blood and Tissue Bank.

Received: ((will be filled in by the editorial staff))

Revised: ((will be filled in by the editorial staff))

Published online: ((will be filled in by the editorial staff))

References

- [1] Carboni EJ. The Margination and Transport of Particles in Blood Flow, Degree Thesis, University of Connecticut, August, 2017.
- [2] Kim P, Ong EH, Li KH, Yoon YJ, Ng SH, Puttachat K. Low-cost, disposable microfluidics device for blood plasma extraction using continuously alternating paramagnetic and diamagnetic capture modes. *Biomicrofluidics*. 2016 Mar 17;10(2):024110.
- [3] Tripathi S, Kumar YB, Agrawal A, Prabhakar A, Joshi SS. Microdevice for plasma separation from whole human blood using bio-physical and geometrical effects. *Sci. Rep*. 2016 Jun 9;6:26749.
- [4] Noruz shamsian O, Mohseni A, Mojaddam M. Design of a Micro-Separator for Circulating Tumor Cells (CTCs) from Blood Flow Using Hybrid Pinched Flow Fractionation (PFF) and Dielectrophoresis Methods. *J. Fluid Mech*. 2020 , 10(1): 281-296

- [5] Xiang N, Ni Z. High-throughput blood cell focusing and plasma isolation using spiral inertial microfluidic devices. *Biomed. Microdevices*. 2015 Dec 1;17(6):110.
- [6] Madadi H, Casals-Terré J, Mohammadi M. Self-driven filter-based blood plasma separator microfluidic chip for point-of-care testing. *Biofabrication*. 2015 May 22;7(2):025007.
- [7] Mohammadi M, Madadi H, Casals-Terré J, Sellarès J. Hydrodynamic and direct-current insulator-based dielectrophoresis (H-DC-iDEP) microfluidic blood plasma separation. *Anal. Bioanal. Chem*. 2015 Jun 1;407(16):4733-44.
- [8] Yang S, Ündar A, Zahn JD. A microfluidic device for continuous, real time blood plasma separation. *Lab Chip*. 2006;6(7):871-80.
- [9] Kim B, Choi S. Smart pipette and microfluidic pipette tip for blood plasma separation. *Small*. 2016 Jan;12(2):190-7.
- [10] Shatova TA, Lathwal S, Engle MR, Sikes HD, Jensen KF. Portable, constriction–expansion blood plasma separation and polymerization-based malaria detection. *Ana. Chem*. 2016 Aug 2;88(15):7627-32.
- [11] Kim B, Oh S, You D, Choi S. Microfluidic pipette tip for high-purity and high-throughput blood plasma separation from whole blood. *Anal. Chem*. 2017 Feb 7;89(3):1439-44.
- [12] Kersaudy-Kerhoas M, Kavanagh DM, Dhariwal RS, Campbell CJ, Desmulliez MP. Validation of a blood plasma separation system by biomarker detection. *Lab Chip*. 2010;10(12):1587-95.
- [13] Prabhakar A, Kumar YB, Tripathi S, Agrawal A. A novel, compact and efficient microchannel arrangement with multiple hydrodynamic effects for blood plasma separation. *Microfluid Nanofluidics*. 2015 May 1;18(5-6):995-1006.
- [14] Li Z, Li X, McCracken B, Shao Y, Ward K, Fu J. A miniaturized hemoretractometer for blood clot retraction testing. *Small*. 2016 Aug;12(29):3926-34.

- [15] Fowler A, Perry DJ. Laboratory monitoring of haemostasis. *Anaesthesia*. 2015 Jan;70:68-e24.
- [16] Santin M, Phillips G. HISTORY OF BIOMIMETIC, BIOACTIVE, AND BIORESPONSIVE BIOMATERIALS. *Biomimetic, Bioresponsive, and Bioactive Materials: An Introduction to Integrating Materials with Tissues*. 2012 Mar 7:1.
- [17] Jigar Panchal H, Kent NJ, Knox AJ, Harris LF. Microfluidics in haemostasis: A review. *Molecules*. 2020 Jan;25(4):833.
- [18] Hickman DA, Pawlowski CL, Sekhon UD, Marks J, Gupta AS. Biomaterials and advanced technologies for hemostatic management of bleeding. *J. Adv. Mater.* 2018 Jan;30(4):1700859.
- [19] Cengel YA. *Fluid mechanics*. Tata McGraw-Hill Education; 2010.
- [20] Karimi S, Mehrdel P, Farré-Lladós J, Casals-Terré J. A passive portable microfluidic blood–plasma separator for simultaneous determination of direct and indirect ABO/Rh blood typing. *Lab Chip*. 2019;19(19):3249-60.
- [21] Karimi S, Farré-Lladós J, Mir E, Escolar G, Casals-Terré J. Hemostasis-on-a-chip: Impedance spectroscopy meets microfluidics for hemostasis evaluation. *MICROMACHINES-BASEL*. 2019 Aug;10(8):534.
- [22] Neeves KB, Onasoga AA, Wufsus AR. The use of microfluidics in hemostasis: clinical diagnostics and biomimetic models of vascular injury. *Curr.* 2013 Sep 1;20(5):417-23.
- [23] Li Z, Li X, McCracken B, Shao Y, Ward K, Fu J. A miniaturized hemoretractometer for blood clot retraction testing. *Small*. 2016 Aug;12(29):3926-34.
- [24] Michelson AD. Methods for the measurement of platelet function. *Am. J. Card.* 2009 Feb 2;103(3):20A-6A.